Automatic Color Image Stitching Using Quaternion Rank-1 Alignment

Jiaxue Li and Yicong Zhou*
Department of Computer and Information Science, University of Macau
Macau, China
lijiaxue7@gmail.com, yicongzhou@um.edu.mo

Abstract

Color image stitching is a challenging task in real-world applications. This paper first proposes a quaternion rank-1 alignment (QR1A) model for high-precision color image alignment. To solve the optimization problem of QR1A, we develop a nested iterative algorithm under the framework of complex-valued alternating direction method of multipliers. To quantitatively evaluate image stitching performance, we propose a perceptual seam quality (PSQ) measure to calculate misalignments of local regions along the seamline. Using QR1A and PSQ, we further propose an automatic color image stitching (ACIS-QR1A) framework. In this framework, the automatic strategy and iterative learning strategy are developed to simultaneously learn the optimal seamline and local alignment. Extensive experiments on challenging datasets demonstrate that the proposed ACIS-QR1A is able to obtain high-quality stitched images under several difficult scenarios including large parallax, low textures, moving objects, large occlusions or/and their combinations.

1. Introduction

Color image stitching refers to the generation of a large image with a broader field of view from multiple partial overlapped color images. As a fundamental task of image processing, it plays a crucial role in diverse applications such as photogrammetry in remote sensing [17], stereoscopic stitching in virtual reality [6] and panoramic stitching in autonomous driving [28]. However, generating high-quality stitched images remains a challenging problem, especially in presence of large parallax, low textures, moving objects, large occlusions or/and their combinations.

Conventionally, the image stitching process contains three steps: first, estimate alignment models to warp input images onto a common coordinate system; second, detect an invisible seam in the overlapping area; third, utilize an image blending technique along this seam to splice aligned images into a larger image. According to the alignment methods in the first step, image stitching works can be broadly classified into feature-based and pixel-based.

In the feature-based methods, the development of image stitching technologies follows two mainstreams: to devise an optimal global alignment, and to search a local alignment enabling an optimal seamline. In the first mainstream, spatially-varying warping methods were proposed to improve the global alignment accuracy [8, 12, 22, 30]. They calculated multiple local adaptive transformations over the whole overlapping area to align images as much as possible. To maintain image naturalness, shape-preserving methods were developed by integrating homography with the similarity transformation [3, 15, 20]. Inspired by content-preserving warping (CPW) [23], the mesh-warping methods were as well as adopted for local adjustments to the alignment accuracy and image naturalness [5, 6, 11, 32]. However, their underlying assumption is that the spatial relations among the neighboring objects should be consistent in different input images. Their estimated local transformations are varied continuously, and hence they perform very well only in presence of small or moderate parallax.

To handle large parallax, the seam-driven strategy was introduced in the second mainstream. The seam-driven methods first estimated local alignment proposals and then selected the optimal one with the best seam quality to create the final stitching result [9, 21, 32]. It's noteworthy that given the same aligned area, different seam calculations usually produce various seamlines such that the stitched images are diverse as well [14]. And the evaluation of seam qualities directly decides the final stitched image. However, these methods put major efforts into generating local alignment proposals while limited considerations on their seamline proposals. Therefore, the simple methods for seamline calculation and evaluation could degrade their final stitching performances implicitly. Additionally, most of them employ the seam quality as a metric to select ready alignment models, instead of guiding the process of alignment model estimation. As a result, the generated best seam from these local alignment proposals cannot guarantee to achieve an

*Corresponding author.

optimal stitching performance.

Interestingly, we further observe a contradictory fact that a plausible seam is usually encouraged to go through the flat regions (*e.g*., sky, walls and roads) whereas the feature-based alignment methods cannot provide the pixel-level accuracy accordingly. In low-textured environments, insufficient features probably lead to the biased estimation of their alignment models, and hence misaligned errors are generated. Such biased estimations may also occur in dynamic scenes where features are distributed non-uniformly due to the moving objects or occlusions. To alleviate this problem, some works explored line features to complement point-feature correspondences [11, 16]. However, the estimated models still perform well in the limited scenes where sufficient line segments should be captured.

To fully utilize image information, pixel-based image alignment methods were developed [18, 19, 26]. They aligned image backgrounds using a low-rank matrix and modeled the misaligned differences among the foregrounds as a sparse matrix. Benefited from this decomposition way, these methods are robust to moving objects and occlusions. Compared with using feature correspondences, they achieve higher alignment accuracy when fitting the same alignment model, especially in low-textured environments. However, when aligning color images, they directly convert color images into grayscale images that ignores the relationship between color channels, resulting in performance degradation.

Motivated by the above limitations, in this paper we introduce an automatic color image stitching method to create high-quality stitched images under kinds of difficult scenarios. Our main contributions are summarized as follows:

1. We propose a quaternion rank-1 alignment (QR1A) model for color image alignment in the quaternion domain. Using the quaternion representation, QR1A is able to fully utilize color image information and obtain high-precision color image alignment results.
2. To solve the optimization problem of QR1A, we develop a nested iterative algorithm under the framework of complex-valued alternating direction method of multipliers.
3. To quantitatively evaluate image stitching performance, we propose a perceptual seam quality (PSQ) measure to calculate misalignments of local regions along the seamline.
4. Using QR1A and PSQ, we further propose an automatic color image stitching (ACIS-QR1A) framework. In this framework, the automatic strategy and iterative learning strategy are developed to simultaneously learn the optimal seamline and local alignment. This offers our ACIS-QR1A the capability of performing high-quality color image stitching automatically.
5. Extensive experiments on different challenging datasets demonstrate that ACIS-QR1A is able to create high-quality stitched images when facing large parallax, low textures, moving objects, large occlusions or/and their combinations.

The rest of this paper is organized as follows: Section 2 reviews the related work. Section 3 proposes the QR1A model and deduces its optimal solution. Section 4 proposes the PSQ measure. Section 5 proposes the ACIS-QR1A framework in detail. Section 6 presents the experiments and comparisons. Finally, Section 7 gives the conclusions.

2. Related Work

Feature-based methods Promoted by advances in feature detection and matching, most of the current works are feature-based. Gao *et al*. proposed a dual-homography model to align images containing two predominant planes [8]. Lin *et al*. computed an affine stitching field whose deviation from the global affine was smoothly varying [22]. Considering the affine model was unable to achieve perspective transformation, Zaragoza *et al*. proposed a moving direct linear transformation to estimate the as-projective-as-possible (APAP) warp which was composed of spatially weighted homographies [30]. Li *et al*. proposed a robust elastic (robust ELA) warping model that formulated the image deformation as the thin plate spline [12]. In low-textured environments, Li *et al*. proposed a dual-feature method to estimate the warping model using both feature points and line segments [16]. To further preserve image structures in wide-parallax condition, Jia *et al*. proposed a joint matching strategy leveraging the line-point consistence (LPC) measure [11]. Nie *et al*. proposed an unsupervised deep image stitching method to handle low-textured images having few hand-craft features [24]. In contrast to stressing the global alignment quality, Gao *et al*. first proposed the seam-driven strategy to align images using a local alignment with the best seam quality [9]. Considering aligned image overlaps will be cut through by this seam, perfect global alignment over the whole overlapping area is actually not necessary. Based on this observation, Zhang and Liu developed a parallax-tolerant method (parallax-tolerant) that first found a local alignment enabling an optimal stitching and then applied the CPW method to refine the global alignment quality [32]. To improve seamline qualities, Lin *et al*. devised a seam-guided scheme (SEAGULL) that reweighted the feature correspondences iteratively to modify their local alignment proposals [21].

Pixel-based methods Theoretically, well-aligned images of the same scene are linearly correlated and hence a low-rank structure can be extracted. Peng *et al*. sought an optimal set of alignment models by decomposing transformed images into a low-rank matrix plus a sparse matrix [26]. However, they solved the rank minimization problem via convex relaxation and applied it to batch images that were fully overlapped. In the image stitching appli-

cation, input images are usually partial overlapped and the number of images is small such that their method performs poorly. To fit the best geometric transformation for image stitching, Li *et al*. first roughly aligned images to extract the overlapping area where then a low-rank matrix was approximated under the non-convex constraint [18]. As an extension, they further proposed a bundle robust alignment and stitching (BRAS) algorithm in which the low-rank component was substituted with an exact rank constraint to optimize their alignment model [19]. However, they converted color images into grayscale images such that the correlated color information among RGB channels was lost. Considering this problem, we propose QR1A model using quaternion representation to fully utilize color image information for high-precision color image alignment. *To the best of our knowledge, directly aligning color images in the quaternion domain has not been addressed up to now.*

3. Quaternion Rank-1 Alignment

This section proposes the QR1A model for robust color image alignment. We first briefly introduce the quaternion algebra and quaternion representation of color image. Then, we describe the QR1A model and give its optimal solution.

3.1. Preliminaries

Quaternion Algebra As the four-dimensional extension of complex space $\mathbb{C}$, a quaternion number ($\dot{q} \in \mathbb{H}$) consists of one real part and three imaginary parts [10]. It is generally represented as:

$$\dot{q} = a_0 + a_1\mathbf{i} + a_2\mathbf{j} + a_3\mathbf{k}, \tag{1}$$

where $\{a_0, a_1, a_2, a_3\} \in \mathbb{R}$ and $\mathbf{i}, \mathbf{j}, \mathbf{k}$ are imaginary bases following: $\mathbf{ij} = -\mathbf{ji} = \mathbf{k}, \mathbf{jk} = -\mathbf{kj} = \mathbf{i}, \mathbf{ki} = -\mathbf{ik} = \mathbf{j}, \mathbf{i}^2 = \mathbf{j}^2 = \mathbf{k}^2 = \mathbf{ijk} = -1$. When $a_0 = 0$, $\dot{q} = a_1\mathbf{i} + a_2\mathbf{j} + a_3\mathbf{k}$ is a pure quaternion number. The quaternion addition is simply the component-wise addition as that in the complex space. But the quaternion multiplication is non-commutative, *i.e.*, $\dot{q}\dot{p} \neq \dot{p}\dot{q}$. Hence, directly multiplying quaternion vectors or matrices is intractable due to its non-commutative property. [31] converts quaternion matrices to pairs of complex matrices and solves them in the complex domain. Here, we introduce several definitions used in this paper.

Definition 1 (Complex adjoint form) *Given a quaternion matrix $\dot{\mathbf{Q}} = \mathbf{A}_0 + \mathbf{A}_1\mathbf{i} + \mathbf{A}_2\mathbf{j} + \mathbf{A}_3\mathbf{k} \in \mathbb{H}^{m\times n}$, it can be delineated with an ordered pair of complex matrices*

$$\dot{\mathbf{Q}} = \mathbf{C}_0 + \mathbf{C}_1\mathbf{j}, \tag{2}$$

where $\mathbf{C}_0 = \mathbf{A}_0 + \mathbf{A}_1\mathbf{i}$, $\mathbf{C}_1 = \mathbf{A}_2 + \mathbf{A}_3\mathbf{i}$, and $\mathbf{C}_0, \mathbf{C}_1 \in \mathbb{C}^{m\times n}$. Then the complex adjoint form of $(\mathbf{C}_0, \mathbf{C}_1)$ uniquely determines $\dot{\mathbf{Q}}$ as follows:

$$\chi_{\dot{\mathbf{Q}}} = \begin{bmatrix} \mathbf{C}_0 & \mathbf{C}_1 \\ -\overline{\mathbf{C}}_1 & \overline{\mathbf{C}}_0 \end{bmatrix} \in \mathbb{C}^{2m\times 2n}. \tag{3}$$

$\dot{\mathbf{Q}}$ and $\chi_{\dot{\mathbf{Q}}}$ are isomorphic [31].

Definition 2 *Given a quaternion vector $\dot{\mathbf{q}} = \mathbf{c}_0 + \mathbf{c}_1\mathbf{j} \in \mathbb{H}^m$, let $\mathbf{q}$ be the first column of $\chi_{\dot{\mathbf{q}}}$, i.e., $\mathbf{q} = \chi_{\dot{\mathbf{q}}}(:, 1) = [\mathbf{c}_0; -\overline{\mathbf{c}}_1] \in \mathbb{C}^{2m}$. The operator $\varsigma(\mathbf{q})$ is defined as:*

$$\varsigma(\mathbf{q}) = \begin{bmatrix} \mathbf{c}_0^T \\ \mathbf{c}_1^T \end{bmatrix} \in \mathbb{C}^{2\times m}. \tag{4}$$

Definition 3 (Quaternion rank [29]) *The rank of a quaternion matrix $\dot{\mathbf{Q}}$ is r if and only if $\dot{\mathbf{Q}}$ has r nonzero singular values, and if and only if the rank of its complex adjoint $\chi_{\dot{\mathbf{Q}}}$ is $2r$.*

Quaternion Representation of Color Image Given a color image I, its quaternion representation $\dot{\mathbf{I}}$ is defined as:

$$\dot{\mathbf{I}}(x, y) = \mathbf{I_r}(x, y)\mathbf{i} + \mathbf{I_g}(x, y)\mathbf{j} + \mathbf{I_b}(x, y)\mathbf{k}, \tag{5}$$

where $\dot{\mathbf{I}}(x, y)$ is the quaternion representation of the color pixel located at (x, y) in the image coordinate system, $\mathbf{I_r}$, $\mathbf{I_g}$ and $\mathbf{I_b}$ denote the red, green and blue channels of the color image I, respectively. Advantages of quaternion representation include: (1) all color components of a color image are encoded together in the quaternion domain; (2) they are capable of being processed simultaneously and holistically, such that the correlated color information among different channels can be fully utilized.

3.2. QR1A Model

Given n color images with a partial overlapping area, their quaternion representations are denoted as $\{\dot{\mathbf{I}}_i\}_{i=1}^n$. We assume that there exist n corresponding geometric transformations $\{\tau_i\}_{i=1}^n$ such that color images from their original coordinate systems can be warped to a common reference coordinate system for alignment. Let $\{\dot{\mathbf{F}}_i\}_{i=1}^n$ be aligned color images, then

$$\dot{\mathbf{F}}_i(x, y) = (\dot{\mathbf{I}}_i \circ \tau_i)(x, y), \tag{6}$$

where $\circ$ denotes image warping and $\tau_i \in \mathbb{R}^{8\times 1}$ is associated with an 8-parameter homography in our work. Subsequently, we extract n overlapped color image areas and vectorize them as columns to stack into a big quaternion matrix. This process is mathematically described as follows:

$$\dot{\mathbf{D}} \circ \tau = [vec(\hat{\dot{\mathbf{F}}}_1), vec(\hat{\dot{\mathbf{F}}}_2), \cdots, vec(\hat{\dot{\mathbf{F}}}_n)] \in \mathbb{H}^{m\times n}, \tag{7}$$

where $\{\hat{\dot{\mathbf{F}}}_i\}_{i=1}^n$ represents aligned image overlaps, $vec(\cdot)$ denotes the operator that linearizes the matrix elements into

a vector, $\dot{\mathbf{D}}$ represents the big quaternion matrix constructed by original image overlaps, $\tau = [\tau_1, \tau_2, \cdots, \tau_n] \in \mathbb{R}^{8\times n}$ and m denotes the number of pixels in the overlapping area.

We here propose a quaternion rank-1 alignment (QR1A) model for color image stitching. The QR1A model is formulated as the following optimization problem:

$$\begin{aligned} &\min_{\dot{\mathbf{L}},\dot{\mathbf{S}},\tau} \|\dot{\mathbf{S}}\|_1 \\ &s.t. \quad \dot{\mathbf{D}} \circ \tau = \dot{\mathbf{L}} + \dot{\mathbf{S}}, \quad rank(\dot{\mathbf{L}}) = 1, \end{aligned} \tag{8}$$

where the quaternion rank-1 matrix $\dot{\mathbf{L}}$ represents the same static backgrounds between the image overlaps (columns). The quaternion sparse matrix $\dot{\mathbf{S}}$ denotes the differences between their foregrounds. It stands for partial artifacts, *e.g.*, moving objects, occlusions and other unavoidable misalignments.

Directly solving the optimization problem in Eq.(8) is quite difficult mainly because the constraint $\dot{\mathbf{D}} \circ \tau = \dot{\mathbf{L}} + \dot{\mathbf{S}}$ is non-linear and the multiplication of quaternions is non-commutative. To solve this non-linear quaternion optimization problem, we reformulate it in the complex space:

$$\begin{aligned} &\min_{\chi_{\dot{\mathbf{L}}},\chi_{\dot{\mathbf{S}}},\triangle\tau} \sum\nolimits_j \|\varsigma(\mathbf{S}_j)\|_{2,1} \\ &s.t. \quad \chi_{\dot{\mathbf{D}}_\tau} + \sum_{i=1}^{n} \chi_{\dot{\mathbf{J}}_i} Re(\triangle\tau \mathbf{e}_i \mathbf{e}_i^T) = \chi_{\dot{\mathbf{L}}} + \chi_{\dot{\mathbf{S}}}, \\ &\quad rank(\chi_{\dot{\mathbf{L}}}) = 2. \end{aligned} \tag{9}$$

where $\chi_{\dot{\mathbf{D}}_\tau}$, $\chi_{\dot{\mathbf{J}}_i}$, $\chi_{\dot{\mathbf{L}}}$ and $\chi_{\dot{\mathbf{S}}}$ are equivalent complex adjoint matrices of $\dot{\mathbf{D}}_\tau$, $\dot{\mathbf{J}}_i$, $\dot{\mathbf{L}}$ and $\dot{\mathbf{S}}$. $\dot{\mathbf{D}}_\tau = \dot{\mathbf{D}} \circ \tau$ for brevity, $\dot{\mathbf{J}}_i = \frac{\partial}{\partial \xi} vec(\dot{\mathbf{I}}_i \circ \xi) \mid_{\xi=\tau_i} \in \mathbb{H}^{m\times 8}$ is the quaternion Jacobian matrix of the ith color image *w.r.t.* its transformation parameters τ_i, $\triangle\tau = [\triangle\tau_1, \triangle\tau_2, \ldots, \triangle\tau_n] \in \mathbb{R}^{8\times n}$ denotes local variations of the current τ, $\{\mathbf{e}_i\}_{i=1}^n$ are the standard basis vectors in $\mathbb{R}^n$, and $Re(\cdot)$ is the operator that constrains inside variables to be real-valued. $\dot{\mathbf{S}}_j$ stands for the jth column of the quaternion matrix $\dot{\mathbf{S}}$, and $\mathbf{S}_j$ is the first column of $\chi_{\dot{\mathbf{S}}_j}$.

3.3. Optimization

To solve the optimization problem in Eq.(9), we develop a nested iterative algorithm. Specifically, we first form the augmented Lagrangian function of Eq.(9):

$$\begin{aligned} &L_\rho(\mathbf{L}, \mathbf{S}, \triangle\tau, \mathbf{Y}) = \sum\nolimits_j \|\varsigma(\mathbf{S}_j)\|_{2,1} \\ &+ Re(Tr(\mathbf{Y}^H[\mathbf{D}_\tau + \sum_{i=1}^{n} \mathbf{J}_i Re(\triangle\tau \mathbf{e}_i \mathbf{e}_i^T) - \mathbf{L} - \mathbf{S}])) \\ &+ \frac{\rho}{2}\|\mathbf{D}_\tau + \sum_{i=1}^{n} \mathbf{J}_i Re(\triangle\tau \mathbf{e}_i \mathbf{e}_i^T) - \mathbf{L} - \mathbf{S}\|_F^2 \\ &s.t. \quad rank(\mathbf{L}) = 2, \end{aligned} \tag{10}$$

where $Tr(\cdot)$ means the trace of a matrix, $\mathbf{Y} \in \mathbb{C}^{2m\times 2n}$ is the Lagrangian multiplier, $\rho > 0$ is the penalty parameter. Here, we let $\mathbf{L} = \chi_{\dot{\mathbf{L}}}$, $\mathbf{S} = \chi_{\dot{\mathbf{S}}}$, $\mathbf{Y} = \chi_{\dot{\mathbf{Y}}}$, $\mathbf{J} = \chi_{\dot{\mathbf{J}}}$, and $\mathbf{D}_\tau = \chi_{\dot{\mathbf{D}}_\tau}$ for brevity. To minimize Eq.(10), we iteratively update each variable against the other fixed variables under the complex ADMM framework [13]. The alternating minimization scheme is presented as follows:

$$\mathbf{L}_{k+1} = \arg\min_{\mathbf{L}:rank(\mathbf{L})=2} L_\rho(\mathbf{L}, \mathbf{S}_k, \triangle\tau_k, \mathbf{Y}_k), \tag{11}$$

$$\mathbf{S}_{k+1} = \arg\min_{\mathbf{S}} L_\rho(\mathbf{L}_{k+1}, \mathbf{S}, \triangle\tau_k, \mathbf{Y}_k), \tag{12}$$

$$\triangle\tau_{k+1} = \arg\min_{\triangle\tau_k} L_\rho(\mathbf{L}_{k+1}, \mathbf{S}_{k+1}, \triangle\tau, \mathbf{Y}_k), \tag{13}$$

$$\mathbf{Y}_{k+1} = \mathbf{Y}_k + \rho[\mathbf{D}_\tau + \sum_{i=1}^{n} \mathbf{J}_i Re(\triangle\tau_{k+1} \mathbf{e}_i \mathbf{e}_i^T) - \mathbf{L}_{k+1} - \mathbf{S}_{k+1}]. \tag{14}$$

Each step in the above scheme involves solving a specific subproblem *w.r.t* a certain variable. In the following, we spell out the closed-form solution for each subproblem.

Update $\mathbf{L}_{k+1}$: We define a quaternion rank-1 projection operator $\Gamma_1 : \mathbb{H}^{m\times n} \to \mathbb{H}^{m\times n}$ as:

$$\Gamma_1\{\dot{\mathbf{Q}}\} = \dot{\mathbf{U}}_1 \sigma_1 \dot{\mathbf{V}}_1^*, \tag{15}$$

where σ_1 is the largest singular value of $\dot{\mathbf{Q}}$ and $\dot{\mathbf{U}}_1 \in \mathbb{H}^m$, $\dot{\mathbf{V}}_1 \in \mathbb{H}^n$ are the corresponding left and right quaternion singular vectors, respectively. The optimal $\dot{\mathbf{L}}_{k+1}$ is obtained at:

$$\dot{\mathbf{L}}_{k+1} = \Gamma_1\{\dot{\mathbf{D}}_\tau + \sum_{i=1}^{n} \dot{\mathbf{J}}_i Re(\triangle\tau \mathbf{e}_i \mathbf{e}_i^T) - \dot{\mathbf{S}}_k + \frac{\dot{\mathbf{Y}}_k}{\rho}\}. \tag{16}$$

We perform the quaternion singular value decomposition in the complex space [4] and construct $\chi_{\dot{\mathbf{L}}_{k+1}}$ to update $\mathbf{L}_{k+1}$.

Update $\mathbf{S}_{k+1}$: We learn the optimum via optimizing its independent column vectors $\mathbf{S}_j$. Due to the redundant structure of the complex adjoint form, we optimize the columns of only the front half part of the matrix:

$$\begin{aligned} &\mathbf{S}_j = \arg\min_{\mathbf{S}_j} \|\varsigma(\mathbf{S}_j)\|_{2,1} + \rho\|\mathbf{S}_j - \mathbf{R}_j\|_2^2 \\ &\text{for} \quad j = 1, 2, \ldots, n. \end{aligned} \tag{17}$$

Here, $\mathbf{R} = \mathbf{D}_\tau + \sum_{i=1}^{n} \mathbf{J}_i Re(\triangle\tau_k \mathbf{e}_i \mathbf{e}_i^T) - \mathbf{L}_{k+1} + \frac{\mathbf{Y}_k}{\rho}$. To separate $\mathbf{S}_j$ from the operator $\varsigma(\cdot)$, we utilize the variable-splitting technique [2] by introducing an auxiliary variable $\mathbf{Z} = \varsigma(\mathbf{S}_j)$ to solve it as follows:

$$\begin{aligned} &\min_{\mathbf{S}_j} \rho\|\mathbf{S}_j - \mathbf{R}_j\|_2^2 + \|\mathbf{Z}\|_{2,1} \\ &s.t. \quad \mathbf{Z} = \varsigma(\mathbf{S}_j). \end{aligned} \tag{18}$$

To solve the subproblem in Eq.(18), we further form its corresponding augmented Lagrangian function:

$$\begin{aligned} &L_\mu(\mathbf{S}_j, \mathbf{Z}, \mathbf{y}) = \rho\|\mathbf{S}_j - \mathbf{R}_j\|_2^2 + \|\mathbf{Z}\|_{2,1} \\ &+ Re(\mathbf{y}^H \left[\mathbf{S}_j - \varsigma^{-1}(\mathbf{Z})\right]) + \frac{\mu}{2}\|\mathbf{S}_j - \varsigma^{-1}(\mathbf{Z})\|_2^2, \end{aligned} \tag{19}$$

where $\mathbf{y} \in \mathbb{C}^{2m}$ is the Lagrangian multiplier, $\mu > 0$ is the penalty parameter and $\varsigma^{-1}(\cdot)$ denotes the inverse operator of $\varsigma(\cdot)$: $\mathbb{C}^{2\times m} \rightarrow \mathbb{C}^{2m}$. Then, the complex ADMM iterations of the sub-algorithm are devised as follows:

$$\mathbf{S}_j^{t+1} = \arg\min_{\mathbf{S}_j} L_\mu(\mathbf{S}_j, \mathbf{Z}^t, \mathbf{y}^t), \tag{20}$$

$$\mathbf{Z}^{t+1} = \arg\min_{\mathbf{Z}} L_\mu(\mathbf{S}_j^{t+1}, \mathbf{Z}, \mathbf{y}^t), \tag{21}$$

$$\mathbf{y}^{t+1} = \mathbf{y}^t + \mu\left[\mathbf{S}_j^{t+1} - \varsigma^{-1}(\mathbf{Z}^{t+1})\right]. \tag{22}$$

Setting the derivatives of Eq. (20) *w.r.t* $\mathbf{S}_j$ to zeros, we update $\mathbf{S}_j^{t+1}$ as follows:

$$\mathbf{S}_j^{t+1} = \left\{ \frac{\rho\mathbf{R}_j^H + \frac{\mu}{2}\left[\varsigma^{-1}(\mathbf{Z}^t) - \frac{\mathbf{y}^t}{\mu}\right]^H}{\rho + \frac{\mu}{2}} \right\}^H. \tag{23}$$

The Eq. (21) can be reduced as follows:

$$\begin{aligned}
&\min_{\mathbf{Z}} \|\mathbf{Z}\|_{2,1} \\
&+ Re((\mathbf{y}^t)^H\left[\mathbf{S}_j^{t+1} - \varsigma^{-1}(\mathbf{Z})\right]) + \frac{\mu}{2}\|\mathbf{S}_j^{t+1} - \varsigma^{-1}(\mathbf{Z})\|_2^2 \\
&= \min_{\mathbf{Z}} \frac{1}{2}\|\mathbf{Z} - \varsigma(\mathbf{S}_j^{t+1} + \frac{\mathbf{y}^t}{\mu})\|_F^2 + \frac{1}{\mu}\|\mathbf{Z}\|_{2,1}.
\end{aligned} \tag{24}$$

Next, we update $\mathbf{Z}^{t+1}$ applying the soft thresholding approach in Lemma 1 [2, 13].

Lemma 1 *Let $\mathbf{X} \in \mathbb{C}$ be a complex-valued variable to the problem:*

$$\min_{\mathbf{X}} \quad \frac{1}{2}\|\mathbf{X} - \mathbf{B}\|_F^2 + \lambda\|\mathbf{X}\|_{2,1}. \tag{25}$$

There exists optimal $\hat{\mathbf{X}}$ satisfying

$$\hat{\mathbf{X}}(:,i) = \begin{cases} \frac{\|\mathbf{B}(:,i)\|_2 - \lambda}{\|\mathbf{B}(:,i)\|_2}\mathbf{B}(:,i), & \|\mathbf{B}(:,i)\|_2 > \lambda \\ 0, & \textit{otherwise.} \end{cases} \tag{26}$$

In the Eq.(22), we can directly update $\mathbf{y}^{t+1}$ using the fixed $\mathbf{S}_j^{t+1}$ and $\mathbf{Z}^{t+1}$. Once the front n column vectors are optimized, the latter half part of $\mathbf{S}_j (j = n+1, \ldots, 2n)$ can be deduced from the structure of complex adjoint form. Sequentially, the optimization for $\mathbf{S}_{k+1}$ is completed.

Update $\triangle\tau_{k+1}$: We calculate the optimum as follows:

$$\begin{aligned}
\triangle\tau_{k+1} &= \arg\min_{\triangle\tau_k} \frac{\rho}{2}\|\sum_{i=1}^{n}\mathbf{J}_i Re(\triangle\tau\mathbf{e}_i\mathbf{e}_i^T) + \mathbf{D}_\tau \\
&\quad - \mathbf{L}_{k+1} - \mathbf{S}_{k+1} + \frac{\mathbf{Y}_k}{\rho}\|_F^2 \\
&= \sum_{i=1}^{n} Re\left(J_i^\dagger(\mathbf{L}_{k+1} + \mathbf{S}_{k+1} - \mathbf{D}_\tau - \frac{\mathbf{Y}_k}{\rho})\mathbf{e}_i\mathbf{e}_i^T\right),
\end{aligned} \tag{27}$$

where $J_i^\dagger$ denotes the Moore-Penrose inverse of complex matrix J_i.

Update $\mathbf{Y}_{k+1}$: We fix the current optimized $\mathbf{L}_{k+1}$, $\mathbf{S}_{k+1}$ and $\triangle\tau_{k+1}$ to update $\mathbf{Y}_{k+1}$ according to Eq.(14).

This alternating minimization algorithm proceeds until the stopping criterion is met. We calculate the primal residual, *i.e.*, $r_{k+1} = \mathbf{D}_\tau + \sum_{i=1}^{n}\mathbf{J}_i Re(\triangle\tau_{k+1}\mathbf{e}_i\mathbf{e}_i^T) - \mathbf{L}_{k+1} - \mathbf{S}_{k+1}$, and the stopping criterion is satisfied when the Frobenius norm of r_{k+1} approaches to zero. Finally, we obtain all closed-form solutions to Eq.(10). It's notable that the linearization in Eq.(9) only holds locally. To learn the final optimal transformation, we will update $\tau \leftarrow \tau + \triangle\tau$ iteratively under the framework of ACIS-QR1A proposed in Section 5.

4. Perceptual Seam Quality Measure

To effectively discriminate different seamlines and precisely evaluate image stitching performance, this section proposes the PSQ measure.

To begin with, for each pixel on the seamline, we extract a local patch (15×15 pixels) centered at it. Since before image composition, the position of each patch corresponds to two overlapped patches from input images, *i.e.*, the reference and target image patches. Then, we calculate visible errors between these overlapped patches to quantify the local misalignments. Inspired by [14], we estimate these errors based on human visual system in which the human's nonuniform attention to complex scenes and nonlinear perception for color differences are investigated.

Specifically, considering pixels with higher saliency values attract more visual attention, we calculate the saliency map for each pair of overlapped patches based on the fast minimum barrier distance (FastMBD) transform [33]. The value of FastMBD at the pixel $\mathbf{p}$ in image patch $\mathbf{P}$ is defined as:

$$d(\mathbf{p}) = \min_{\phi\in\Phi}\left[\max_{k=0}^{n}\mathbf{P}(\phi(k)) - \min_{k=0}^{n}\mathbf{P}(\phi(k))\right], \tag{28}$$

where $\phi = \{\phi(0), \phi(1), \ldots, \phi(n)\}$ is a path composed of a sequence of adjacent pixels, Φ is the set of paths that connect the pixel $\mathbf{p}$ to the boundary pixels of its left neighbor and upper neighbor, respectively. Then, the color difference is weighted *w.r.t.* the corresponding pixel saliency. That is, the color differences will be highlighted in salient regions while suppressed in non-salient regions. To human eyes, only when the stimulus is larger than a threshold can the color difference be noticed. Besides, the sensitivity to the perceived color difference is changed nonlinearly. As the stimulus is enhanced, the visual discrimination will decrease. We characterize this nonlinear perception process as a sigmoid curve.

Consolidating the above models, we define the percep-

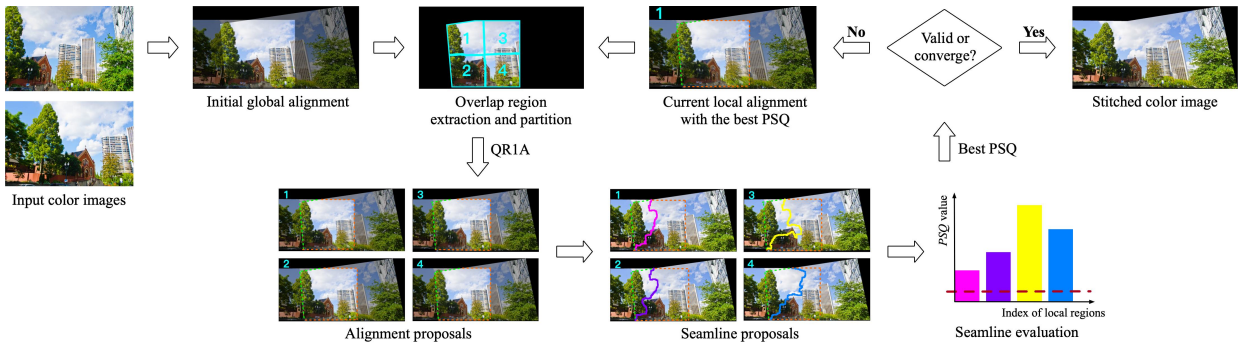

Figure 1. The proposed ACIS-QR1A framework.

tual quality of a seam as follows:

$$E_{PSQ} = \frac{1}{MN}\sum_{i=1}^{M}\sum_{j=1}^{N}\frac{1}{1+\exp(-\beta(\mathbf{W}_{ij}\,|\mathbf{P}_{ij}-\mathbf{Q}_{ij}|-\alpha))}, \tag{29}$$

where $\mathbf{W}_{ij} = d(\mathbf{P}_{ij}) + d(\mathbf{Q}_{i,j})$. $\mathbf{W}_{ij}$, $\mathbf{P}_{ij}$ and $\mathbf{Q}_{ij}$ are the values of jth pixel in the ith patch of the saliency matrix, reference image patch and target image patch, respectively. M, N denote the numbers of total patches and the pixels contained per patch, respectively. α and β are constants controlling the thresholds of recognizing the color difference and the sensitivity stimulated by that discrimination, respectively. We calculate α and β using the Ostu's algorithm [25]. The value of E_{PSQ} has been normalized to the range of $[0, 1]$. Generally, the smaller value indicates the better seam quality and better stitching performance.

5. Automatic Color Image Stitching Framework

As shown in Fig. 1, we utilize the QR1A model and PSQ measure to further propose an automatic color image stitching framework called ACIS-QR1A in this section.

The essence of our framework is to accurately align a suitable local region such that a high-quality seamline is generated for color image stitching. To this end, we develop the automatic strategy and iterative learning strategy for this framework. In contrast to the conventional pipeline that calculates alignment and seamline sequentially and independently, the automatic strategy argues to merge the processes of alignment estimation and seamline detection together such that the optimal stitching performance is obtained in a holistic way. Meanwhile, the iterative learning strategy is devised to learn the optimal seamline and local alignment simultaneously in an iterative manner.

Specifically, we first roughly align images using an initial global homography [7]. Then, the overlapping area is extracted and partitioned into separate local regions employing the segmentation technique [1]. In each local region, we learn an alignment proposal using the QR1A optimization algorithm. Next, the seam-cutting technique [14] is carried out to generate a seamline proposal accordingly. We use the PSQ measure to evaluate the perceptual stitching qualities of all seamline proposals. To choose a suitable local region for stitching, we select the alignment proposal with the best PSQ and make it the initial alignment for the next iteration. Under the guidance of PSQ, alignment proposals in the following iterations are optimized by QR1A towards the direction of the best stitching performance. Meanwhile, the PSQ values of seamline proposals are optimized as well. In each iteration, both the current optimal local alignment and seamline are updated adaptively. The iteration proceeds until the optimized seamline meets the predetermined PSQ standard (red dots in the histogram) or the relative difference of PSQ values between two consecutive iterations is lower than a threshold (10^{-4}).

6. Experiments

We first perform an ablation study to demonstrate the effectiveness of QR1A model and the iterative learning strategy in ACIS-QR1A framework, respectively. We then compare the overall color image stitching performance of ACIS-QR1A with that of the state-of-the-art methods on challenging public datasets, quantitatively and qualitatively. In the QR1A optimization algorithm, we set initial variables $\mathbf{L}_0, \mathbf{S}^0, \mathbf{Z}^0, \triangle\tau, \mathbf{Y}_0, \mathbf{y}^0, k$ and t equal to 0, ρ and μ equal to 1.25. The stopping threshold is set to 10^{-5} empirically.

6.1. Ablation Study

We perform ablation experiments on the *009 dataset* [32] where parallax and moving kids exist. In ACIS-QR1A, we segment the overlapping area into five local regions. Accordingly, five local alignment proposals and five seamline proposals are generated in each iteration. For clarity, the seamline color indicates images are stitched on different local alignment proposals. To explore the iterative learning process of ACIS-QR1A, we present the intermediate stitched results of each iteration. For comparison, the initial

global alignment result is directly composed as the baseline. We then construct an experiment following the traditional step-by-step pipeline, in which images are first iteratively aligned by QR1A, and then composed sequentially.

As shown in Fig. 2, artifacts occur easily due to the local misaligned areas along the seamline. The stitched result using the initial global alignment in Fig. 2(a) suffers from obvious artifacts in many local regions. By introducing QR1A in Fig. 2(b), the severe artifacts are largely relieved, but there still exist slight errors that cannot be precisely aligned in presence of parallax. In Fig. 2(c), the iterative process of ACIS-QR1A is illustrated and the changing seamline color denotes that the local alignment is optimized dynamically under the guidance of PSQ. From these magnified regions, it can be observed that those circled artifacts are rectified iteratively until they are totally vanished along the seamline. Even in the sky, the slight ghosting artifacts can also be detected and rectified.

6.2. Performance Comparison

The overall color image stitching performance of ACIS-QR1A is compared with the global homography (baseline) and the state-of-the-art methods including APAP [30], robust ELA [12], LPC [11], parallax-tolerant [32], SEAGULL [21] and BRAS [19]. The qualitative and quantitative results are from papers or generated by their released codes. For fairness in comparison, we uniformly adopt the perception-based seam cutting [14] and Poisson blending technique [27] to compose their aligned images.

Qualitative Evaluation To fully evaluate the color image stitching ability, we compare different algorithms analyzing four typical challenging datasets.

1) Large Parallax: A typical example is the *025 dataset* [32] in which the spatial relations of the lorry, the chimney and the tree are different between input images. In Fig. 3, it can be observed that both APAP and robust ELA distort images due to such inconsistent spatial distribution, despite per feature correspondence established accurately. Slight distortions and misalignments are also generated in other methods, except the LPC and ACIS-QR1A.

2) Moving Objects: In the *071 dataset* [32], the streams of cars at the crossroads disturb the uniform distribution of features and may also introduce inconsistent spatial distribution of matched features. From Fig. 4, we can observe that both APAP and robust ELA distort the middle and right buildings severely. Original three lanes in input images are duplicated to four lanes in other feature-based results. BRAS suffers from slight misalignments of lines on the roads. ACIS-QR1A is free from these artifacts.

3) Low Textures: As shown in Fig. 5, stitching images with few textures is difficult especially for the feature-based methods. In BRAS, slight misalignments in the shadows are magnified. By contrast, ACIS-QR1A is able to align these regions precisely for color image stitching.

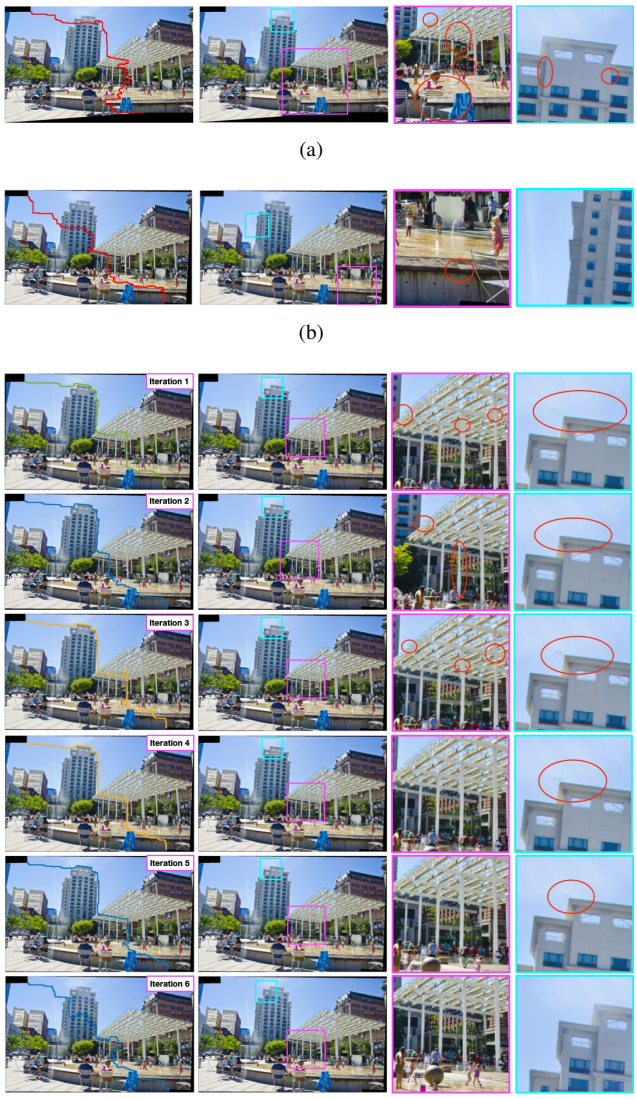

(a)

(b)

(c)

Figure 2. Stitched results using (a) the initial global alignment, (b) QR1A, (c) the iterative learning strategy of ACIS-QR1A.

4) Large Occlusions: In the *catabus dataset* [19], the background is occluded by a moving bus such that most feature correspondences are established among the moving bus. That is, if the feature-based methods rely on both the moving features and static features, distortions and artifacts are generated easily. We can observe both APAP and robust ELA distort images severely. Original one tree in input images is duplicated in all feature-based results. BRAS and ACIS-QR1A are able to achieve good performance.

Quantitative Evaluation To precisely compare image stitching performance, different algorithms are equally evaluated with the same PSQ metric. Table 1 records the PSQ

Figure 3. Comparison of different algorithms on the *025 dataset* [32]: the case with large parallax.

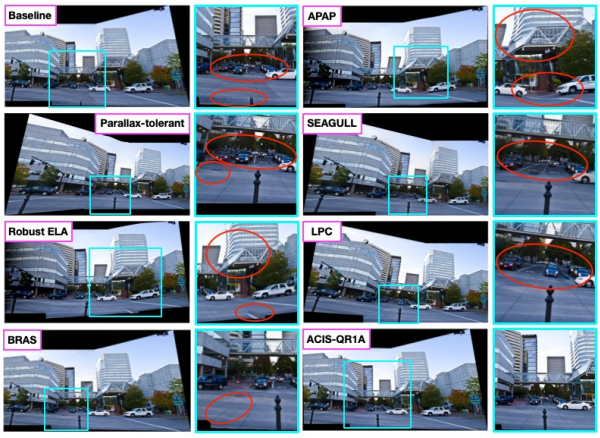

Figure 4. Comparison of different algorithms on the *071 dataset* [32]: the case with moving objects and parallax.

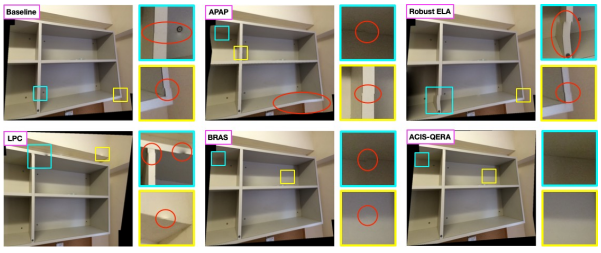

Figure 5. Comparison of different algorithms on the *shelf dataset* [16]: the case with low textures and parallax.

values of different algorithms on 20 challenging datasets. The best scores are highlighted in bold. We can observe that our ACIS-QR1A outperforms other methods almost consistently. Meanwhile, the high-precision local alignment along the seamline is demonstrated, especially in No.11 to No.15 cases (low textures and parallax). Notice that although robust ELA obtains the better PSQ in No.18 case, its stitched

Figure 6. Comparison of different algorithms on the *catabus dataset* [19]: the case with large occlusions and parallax.

image suffers from severe distortions due to the moving objects and large parallax. We provide the corresponding qualitative results in the supplementary material.

No.	Dataset	Baseline [14]	APAP [30]	Robust ELA [12]	LPC [11]	BRAS [19]	ACIS-QR1A
1	*temple* [8]	0.1388	0.1846	0.1242	0.1614	0.1089	**0.0004**
2	*069* [32]	0.1418	0.0691	0.0849	0.0648	0.0609	**0.0191**
3	*05* [21]	0.0625	0.0603	0.1278	0.0436	0.0417	**0.0352**
4	*13* [21]	0.0345	0.0872	0.0706	0.0516	0.0287	**0.0158**
5	*24* [21]	0.0923	0.1276	0.1454	0.181	0.0724	**0.0326**
6	*025* [32]	0.0823	0.0692	0.0485	0.0647	0.0177	**0.0137**
7	*053* [32]	0.0984	0.1092	0.099	0.1111	0.0703	**0.0563**
8	*059* [32]	0.1134	0.0374	0.1539	0.0308	0.029	**0.0107**
9	*073* [32]	0.0848	0.0852	0.135	0.1073	0.0895	**0.0448**
10	*001* [32]	0.0044	0.0021	0.0022	0.0091	0.0043	**0.0010**
11	*corner* [16]	0.1452	0.3778	0.3232	0.0061	0.1268	**0.0004**
12	*roof* [16]	0.1677	0.1533	0.1046	0.0162	0.1257	**0.0002**
13	*four* [16]	0.2140	0.0974	0.4214	0.1013	0.1151	**0.0742**
14	*cabinet* [16]	0.5400	0.5685	0.4942	0.2943	0.4526	**0.00003**
15	*window* [16]	0.2279	0.4148	0.3711	0.2612	0.3664	**0.00003**
16	*009* [32]	0.0719	0.1000	0.0561	0.0692	0.0413	**0.0253**
17	*071* [32]	0.0968	0.1232	0.0756	0.0976	0.0528	**0.0468**
18	*12* [21]	0.0776	0.0816	**0.0185**	0.0847	0.0405	0.0207
19	*17* [21]	0.0200	0.0184	0.0334	0.0998	0.0259	**0.0115**
20	*catabus* [19]	0.0104	0.0159	0.0143	0.0392	0.0002	**0.0001**

Table 1. Comparison of stitching quality using the PSQ measure. No.1 to No.5: small parallax. No.6 to No.10: large parallax and occlusions. No.11 to No.15: low textures and parallax. No.16 to No.20: moving objects, large parallax and occlusions.

7. Conclusions

In this paper, we first proposed QR1A model for high-precision color image alignment in the quaternion domain. To solve the optimization problem of QR1A, we developed a nested iterative algorithm under the complex ADMM framework. We also proposed PSQ measure to precisely evaluate image stitching performance. Using QR1A and PSQ, we further proposed the ACIS-QR1A framework to simultaneously learn the optimal seamline and local alignment. Extensive experiments on challenging datasets demonstrated that the proposed ACIS-QR1A is able to create high-quality stitched images under several difficult scenarios including large parallax, low textures, moving objects, large occlusions or/and their combinations.

References

[1] Radhakrishna Achanta, Appu Shaji, Kevin Smith, Aurelien Lucchi, Pascal Fua, and Sabine Süsstrunk. Slic superpixels compared to state-of-the-art superpixel methods. *IEEE Transactions on Pattern Analysis and Machine Intelligence*, 34(11):2274–2282, 2012. 6

[2] Stephen Boyd, Neal Parikh, and Eric Chu. *Distributed optimization and statistical learning via the alternating direction method of multipliers*. Now Publishers Inc, 2011. 4, 5

[3] Che-Han Chang, Yoichi Sato, and Yung-Yu Chuang. Shape-preserving half-projective warps for image stitching. In *IEEE Conference on Computer Vision and Pattern Recognition*, pages 3254–3261, 2014. 1

[4] Yongyong Chen, Xiaolin Xiao, and Yicong Zhou. Low-rank quaternion approximation for color image processing. *IEEE Transactions on Image Processing*, 29:1426–1439, 2019. 4

[5] Yu-Sheng Chen and Yung-Yu Chuang. Natural image stitching with the global similarity prior. In *European Conference on Computer Vision*, pages 186–201. Springer, 2016. 1

[6] Xiaoting Fan, Jianjun Lei, Yuming Fang, Qingming Huang, Nam Ling, and Chunping Hou. Stereoscopic image stitching via disparity-constrained warping and blending. *IEEE Transactions on Multimedia*, 22(3):655–665, 2019. 1

[7] Martin A Fischler and Robert C Bolles. Random sample consensus: a paradigm for model fitting with applications to image analysis and automated cartography. *Communications of the ACM*, 24(6):381–395, 1981. 6

[8] Junhong Gao, Seon Joo Kim, and Michael S Brown. Constructing image panoramas using dual-homography warping. In *IEEE Conference on Computer Vision and Pattern Recognition*, pages 49–56. IEEE, 2011. 1, 2, 8

[9] Junhong Gao, Yu Li, Tat-Jun Chin, and Michael S Brown. Seam-driven image stitching. In *Eurographics (Short Papers)*, pages 45–48, 2013. 1, 2

[10] William Rowan Hamilton. On quaternions; or on a new system of imaginaries in algebra. *The London, Edinburgh, and Dublin Philosophical Magazine and Journal of Science*, 33(219):58–60, 1848. 3

[11] Qi Jia, ZhengJun Li, Xin Fan, Haotian Zhao, Shiyu Teng, Xinchen Ye, and Longin Jan Latecki. Leveraging line-point consistence to preserve structures for wide parallax image stitching. In *IEEE Conference on Computer Vision and Pattern Recognition*, pages 12186–12195, 2021. 1, 2, 7, 8

[12] Jing Li, Zhengming Wang, Shiming Lai, Yongping Zhai, and Maojun Zhang. Parallax-tolerant image stitching based on robust elastic warping. *IEEE Transactions on Multimedia*, 20(7):1672–1687, 2017. 1, 2, 7, 8

[13] Lu Li, Xingyu Wang, and Guoqiang Wang. Alternating direction method of multipliers for separable convex optimization of real functions in complex variables. *Mathematical Problems in Engineering*, 2015, 2015. 4, 5

[14] Nan Li, Tianli Liao, and Chao Wang. Perception-based seam cutting for image stitching. *Signal, Image and Video Processing*, 12(5):967–974, 2018. 1, 5, 6, 7, 8

[15] Nan Li, Yifang Xu, and Chao Wang. Quasi-homography warps in image stitching. *IEEE Transactions on Multimedia*, 20(6):1365–1375, 2017. 1

[16] Shiwei Li, Lu Yuan, Jian Sun, and Long Quan. Dual-feature warping-based motion model estimation. In *IEEE International Conference on Computer Vision*, pages 4283–4291, 2015. 2, 8

[17] Xinghua Li, Ruitao Feng, Xiaobin Guan, Huanfeng Shen, and Liangpei Zhang. Remote sensing image mosaicking: Achievements and challenges. *IEEE Geoscience and Remote Sensing Magazine*, 7(4):8–22, 2019. 1

[18] Yuelong Li and Vishal Monga. Siasm: Sparsity-based image alignment and stitching method for robust image mosaicking. In *IEEE International Conference on Image Processing*, pages 1828–1832, 2016. 2, 3

[19] Yuelong Li, Mohammad Tofighi, and Vishal Monga. Robust alignment for panoramic stitching via an exact rank constraint. *IEEE Transactions on Image Processing*, 28(10):4730–4745, 2019. 2, 3, 7, 8

[20] Chung-Ching Lin, Sharathchandra U Pankanti, Karthikeyan Natesan Ramamurthy, and Aleksandr Y Aravkin. Adaptive as-natural-as-possible image stitching. In *IEEE Conference on Computer Vision and Pattern Recognition*, pages 1155–1163, 2015. 1

[21] Kaimo Lin, Nianjuan Jiang, Loong-Fah Cheong, Minh Do, and Jiangbo Lu. Seagull: Seam-guided local alignment for parallax-tolerant image stitching. In *European Conference on Computer Vision*, pages 370–385. Springer, 2016. 1, 2, 7, 8

[22] Wen-Yan Lin, Siying Liu, Yasuyuki Matsushita, Tian-Tsong Ng, and Loong-Fah Cheong. Smoothly varying affine stitching. In *IEEE Conference on Computer Vision and Pattern Recognition*, pages 345–352, 2011. 1, 2

[23] Feng Liu, Michael Gleicher, Hailin Jin, and Aseem Agarwala. Content-preserving warps for 3d video stabilization. *ACM Transactions on Graphics*, 28(3):1–9, 2009. 1

[24] Lang Nie, Chunyu Lin, Kang Liao, Shuaicheng Liu, and Yao Zhao. Unsupervised deep image stitching: Reconstructing stitched features to images. *IEEE Transactions on Image Processing*, 30:6184–6197, 2021. 2

[25] Nobuyuki Otsu. A threshold selection method from gray-level histograms. *IEEE Transactions on Systems, Man, and Cybernetics*, 9(1):62–66, 1979. 6

[26] Yigang Peng, Arvind Ganesh, John Wright, Wenli Xu, and Yi Ma. Rasl: Robust alignment by sparse and low-rank decomposition for linearly correlated images. *IEEE Transactions on Pattern Analysis and Machine Intelligence*, 34(11):2233–2246, 2012. 2

[27] Patrick Pérez, Michel Gangnet, and Andrew Blake. Poisson image editing. In *ACM Transactions on Graphics*, pages 313–318. 2003. 7

[28] Lang Wang, Wen Yu, and Bao Li. Multi-scenes image stitching based on autonomous driving. In *IEEE Information Technology, Networking, Electronic and Automation Control Conference*, volume 1, pages 694–698, 2020. 1

[29] Louise A Wolf. Similarity of matrices in which the elements are real quaternions. *Bulletin of the American Mathematical Society*, 42(10):737–743, 1936. 3

[30] Julio Zaragoza, Tat-Jun Chin, Michael S Brown, and David Suter. As-projective-as-possible image stitching with mov-

ing dlt. In *IEEE Conference on Computer Vision and Pattern Recognition*, pages 2339–2346, 2013. 1, 2, 7, 8

[31] Fuzhen Zhang. Quaternions and matrices of quaternions. *Linear Algebra and its Applications*, 251:21–57, 1997. 3

[32] Fan Zhang and Feng Liu. Parallax-tolerant image stitching. In *IEEE Conference on Computer Vision and Pattern Recognition*, pages 3262–3269, 2014. 1, 2, 6, 7, 8

[33] Jianming Zhang, Stan Sclaroff, Zhe Lin, Xiaohui Shen, Brian Price, and Radomir Mech. Minimum barrier salient object detection at 80 fps. In *IEEE International Conference on Computer Vision*, pages 1404–1412, 2015. 5